

A spectrometer for high-precision ion temperature and velocity measurements in low-temperature plasmas

Cite as: Rev. Sci. Instrum. **90**, 063502 (2019); <https://doi.org/10.1063/1.5092966>

Submitted: 15 February 2019 . Accepted: 15 May 2019 . Published Online: 05 June 2019

J. Milhone , K. Flanagan , M. D. Nornberg , M. Tabbutt , and C. B. Forest 

COLLECTIONS

 This paper was selected as an Editor's Pick



[View Online](#)



[Export Citation](#)



[CrossMark](#)

ARTICLES YOU MAY BE INTERESTED IN

[Closed-cycle, low-vibration 4 K cryostat for ion traps and other applications](#)

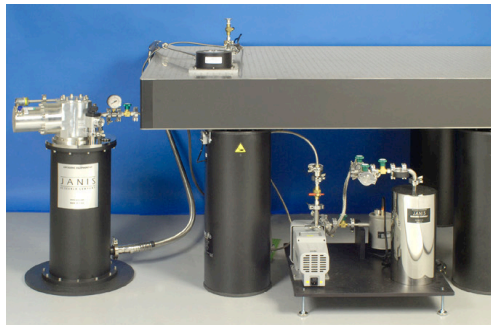
Review of Scientific Instruments **90**, 065104 (2019); <https://doi.org/10.1063/1.5088593>

[A data acquisition system for HV-CMOS sensor research and development in the upgrade of ATLAS experiment](#)

Review of Scientific Instruments **90**, 064701 (2019); <https://doi.org/10.1063/1.5092714>

[A fast key parameter extraction algorithm for long fiber distributed sensing based on Brillouin scattering](#)

Review of Scientific Instruments **90**, 066101 (2019); <https://doi.org/10.1063/1.5049738>



JANIS

Rising LHe costs? Janis has a solution.

Janis' Recirculating Cryocooler eliminates the use of Liquid Helium for "wet" cryogenic systems.

sales@janis.com www.janis.com Click for more information.

A spectrometer for high-precision ion temperature and velocity measurements in low-temperature plasmas

EP

Cite as: Rev. Sci. Instrum. 90, 063502 (2019); doi: 10.1063/1.5092966

Submitted: 15 February 2019 • Accepted: 15 May 2019 •

Published Online: 5 June 2019



View Online



Export Citation



CrossMark

J. Milhone,^{a)} K. Flanagan, M. D. Nornberg, M. Tabbutt, and C. B. Forest

AFFILIATIONS

Department of Physics, University of Wisconsin, Madison, Wisconsin 53706, USA

^{a)}jmilhone@wisc.edu

ABSTRACT

We have developed a low-cost spectrometer with simple optical design that achieves unprecedented precision measurements of ion temperature (± 0.01 eV) and velocity (± 20 m/s). A Fabry-Pérot étalon provides the simultaneous high resolving power and high throughput needed for the light levels available in singly ionized helium and argon plasmas. Reducing the systematic uncertainty in the absolute wavelength calibration needed for the specified velocity precision motivates a Bayesian analysis method called Nested Sampling to address the nontrivial uncertainty in the diffraction order. An initial emission measurement of a singly charged stationary argon plasma yields a temperature of 0.339 ± 0.007 eV and a velocity of -3 ± 4 m/s with a systematic uncertainty of 20 m/s.

Published under license by AIP Publishing. <https://doi.org/10.1063/1.5092966>

I. INTRODUCTION

Many processes and behaviors of low-temperature plasmas are heavily influenced by ion dynamics. Some examples include sheath expansion by warm ions,^{1,2} atmospheric pressure plasmas and their medical applications for ions near room temperature,³ and the transport of momentum via kinematic viscosity in flowing plasmas. In each of these examples, it is extremely important to have a measurement of the ion temperature and velocity distribution in order to correctly predict and model behavior. In the case of flowing plasmas, Braginskii⁴ developed a formula for kinematic viscosity using collisional theory showing that the momentum of an unmagnetized plasma diffuses at a rate set by the ion thermal speed, v_{Ti} , and the ion-ion collision time, τ_{ii} . This combination of terms results in a particularly strong, $T_i^{5/2}$, dependence on the ion temperature. Propagating the error of a given ion temperature measurement to the resulting viscosity illustrates the need for precise measurements for estimating the theoretical value. For example, a singly charged argon plasma with an ion temperature relative uncertainty of 10% and an electron density relative uncertainty of 10% (both reasonable uncertainties for well-diagnosed laboratory plasmas) yields a 27% uncertainty in the theoretical value of Braginskii viscosity. This level of error can greatly affect results of modeling flows in experimental

data.⁵ In a similar fashion, the viscosity can be experimentally determined from spatially resolved measurements of velocity that require accurate flow measurements. Motivated by the desire for accurate viscosity measurements and the ability to compare with theory, we have developed a high precision velocity and ion temperature diagnostic, which is applicable to many other low-temperature plasma applications.

Measurements of ion temperature and ion flow in the low-temperature regime can be quite challenging. Traditionally, basic plasma experiments have been diagnosed with probes inserted into the plasma. The flow velocity can be measured with a Mach probe^{6–9} and interpreted as an absolute velocity using the local sound speed measured by a Langmuir probe. The ion temperature is more difficult to measure with a probe. Retarded field energy analyzers (RFEA)^{10–12} can be used to measure the ion energy distribution function directly, but shielding out the electrons is difficult. Probes can also be detrimental to the plasma performance by increasing loss area, sputtering of particles, and outgassing leading to a decrease in conductivity and an increase in neutral drag. Laser induced fluorescence (LIF)^{13,14} is another option, but it is expensive, more complicated, and has low time resolution. In addition, it is possible for the metastables to be produced from ionization instead of from ground state excitation.¹⁵ Ion temperature and flows can be measured

noninvasively by using optical diagnostics that are sensitive to both velocity and velocity shear. Straight forward measurements of ion emission require high resolution spectrometers and can suffer from lack of light with insufficient étendue.

In this paper, we describe a high-throughput and simple-to-implement spectrometer capable of measuring the very small Doppler shifts and broadening of low-temperature plasmas, using a Fabry-Pérot étalon and a digital camera. Previous measurements with the Fabry-Pérot spectrometer demonstrated the ability to measure ion temperatures as low as room temperature up to a few electron volts.^{16,17} A redesign of the system including the use of a high numerical aperture fiber and collimator and a rail mounted optical assembly has resulted in a higher étendue spectrometer that is easy to align and is portable between the different laboratory spaces at the Wisconsin Plasma Physics Laboratory (WiPPL).¹⁶

This paper is organized as follows: Section II describes the design considerations for a high-resolution and high-throughput Fabry-Pérot spectrometer. Recent upgrades to the spectrometer including an optical rail mount system and a large numerical aperture fiber will be discussed. Section III goes into the details of analyzing the data from the spectrometer. Section III A describes the initial image preprocessing to obtain intensity as a function of pixel radius. Section III B goes into details regarding absolute wavelength and point spread function (PSF) calibration as well as the need for a Bayesian approach to determine calibration parameters to sufficient accuracy for measuring T_i to ± 0.01 eV and V to ± 20 m/s. Section III C describes the analysis routine for plasma data. Section IV presents preliminary results for argon plasmas.

II. DESIGN CONSIDERATIONS FOR HIGH RESOLUTION SPECTROSCOPY

Measuring ion temperatures below a few electron volts and velocities below 10 km/s spectroscopically in the visible range requires a spectrometer with a resolution of the order of a picometer. For low electron temperature plasmas ($T_e < 10$ eV) at moderate densities ($n_e \approx 10^{18}$ m⁻³), ion emission in the visible spectrum is weak. Measurements could be made in the vacuum ultraviolet (VUV), but then the spectrometer becomes an integral part of the vacuum vessel which can complicate adjustments and calibration. The combination of low radiance and the need to resolve ion equilibrium time dynamics sets the requirements for the light gathering capability of the diagnostic. These requirements can be satisfied by a traditional grating spectrometer, but a Fabry-Pérot spectrometer is more compact and has a simpler optical design that can be implemented at lower cost.

One of the first design considerations is the spatial resolution of the chord measurement. For typical plasmas at the WiPPL, the electron density and temperature is uniform, except for a steep edge gradient. For expected ion temperatures, the velocity gradient scale length is on the order of about 30 cm, so the spatial resolution requirements are modest. Therefore, the maximum optical throughput is set only by the optical access to the plasma which is constrained by the magnet spacing and port size. The magnet spacing allows the use of two-inch collection optics which provide adequate light collection with sufficient resolution of velocity gradients. The light is collimated by the collection optics and transmitted over a fiber to the spectrometer. The collimator is attached to a linear stage

mounted on a box port with a large window to allow many different views of the plasma cross section and to decouple the alignment of the diagnostic from the plasma view. To maximize the light collection, a large core diameter, high-NA fiber was chosen to maximize the étendue, $G = \pi S(NA)^2$. A multifiber bundle could also be used, but the packing fraction must be considered. The large NA requires very fast (low $f/ \#$) optics requiring aspherical lenses for collimation to limit spherical aberrations.

The main optical element in a Fabry-Pérot spectrometer is an étalon consisting of two highly reflective parallel plates separated by a small distance d . The high reflectivity allows for light to reflect many times before exiting the cavity. For a given wavelength, λ , the interference condition is given by

$$m\lambda = 2nd \cos \theta \quad m \in 0, 1, \dots, m_0 = \text{Floor}\left(\frac{2nd}{\lambda}\right), \quad (1)$$

where n is the index of refraction of air, θ is the angle that light enters the étalon relative to the optical axis, and m is a non-negative integer less than the maximum order, m_0 . The light exiting the étalon is focused by a lens with focal length f_2 down onto the camera sensor. The measured intensity pattern is a set of concentric rings (see Fig. 1) where the innermost ring corresponds to the maximum order m_0 . The étalon is placed inside an optical telescope where the rays are within a small range of angles from horizontal to achieve the desired ring interference pattern.

The components in the optical assembly are chosen based on a few design criteria. As shown in Fig. 2, the assembly consists of a fiber with a collimator, an optical telescope, an étalon placed inside the telescope, a bandpass filter, and a camera sensor. As discussed earlier, the étendue is set by the fiber and collection optics. The requirements for the detector are quite modest and depend mostly on pixel sensitivity, pixel size, and read noise. As such, the first measurements are conducted with a commercial DSLR camera. The camera lens with focal length f_2 was chosen to have 5 sets of concentric rings such that the central ring of interest is near the optical axis away from any adverse effects such as spherical aberration. The objective lens of the telescope was chosen to match the illuminated part of the lens from the collection optics to the sensor size. The

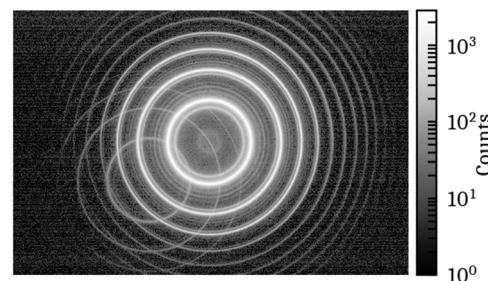
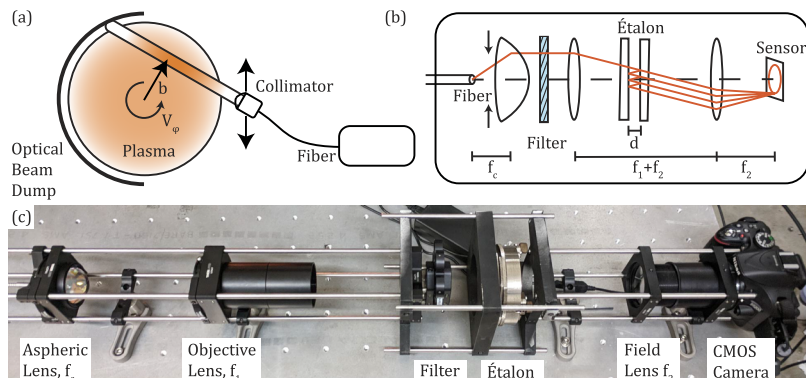


FIG. 1. Fabry-Pérot image of Th Ar-fill hollow cathode lamp. The calibration lamp's complicated spectra in this wavelength range consists of two dominate lines (ThI 487.873 302 nm and ArII 487.986 34 nm)¹⁸ and many low amplitude ThI lines. Contributions from the nuisance lines are mitigated using three Andover 1 nm FWHM bandpass filters at 488 nm. The 3 two-cavity filters provide a ~ 30 dB rejection ratio of wavelengths outside twice the bandpass. The log scale emphasizes the undesirable secondary ring pattern from misalignment.



filter must be placed in a region where the rays have a small angle with respect to the optical axis, otherwise more light than expected will pass through the filter. A picture of the assembled diagnostic is shown in Fig. 2.

Achieving good alignment of the Fabry-Pérot spectrometer is crucial for high spectral resolution. Alignment requires all elements centered on, and perpendicular to, the optical axis. If any of the components are offset from the optical axis, the intensity profile will be shifted from the center of the image plane resulting in rings lacking azimuthal symmetry in intensity. The étalon plates can be made parallel with three adjustment screws controlling the amount of pressure applied via springs. The camera sensor must be placed such that the sensor images at infinity, otherwise the rings will be out of focus and extra Gaussian broadening will need to be accounted for in the analysis. With the high-throughput collection optics, these effects are reduced *in situ* by collecting light from a calibration lamp and observing the ring pattern while adjusting the placement of each optical element.

III. ANALYSIS TECHNIQUES

Section III B outlines the procedure implemented to calibrate the spectrometer using the Bayesian methodology illustrated in Fig. 3. A model for the output image is defined with a set of parameters. A Gaussian probability likelihood function for the parameters given the data is chosen. The constraints from prior information on reasonable parameter ranges are encoded as uniform probability distributions. A Monte Carlo calculation is run which draws samples from the prior distributions and evaluates the likelihood to determine the posterior probability for the parameters given the data. Any extra parameters in the model, such as amplitudes or offsets, are integrated over to give marginal posterior probabilities for the parameters of interest.

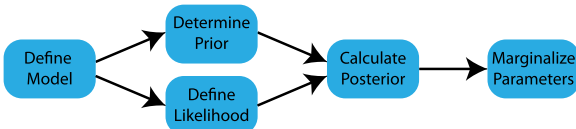


FIG. 3. Procedure for solving a problem with a Bayesian approach.

FIG. 2. (a) Fabry-Pérot optical schematic. Light is collected from the plasma with a f/1.0 collimator mounted on a linear stage to allow scanning of the plasma volume. The chord's closest distance to the origin is labeled by its impact factor, b . An optical beam dump is located on the far side of the vessel to limit the reflected light from entering the collimator. (b) Optical schematic of Fabry-Pérot. (c) Picture of Fabry-Pérot. Light from the fiber is collimated by a f/1.0 collimator and focused by the objective lens ($f_1 = 350$ mm) onto a 5 mm spot size on the étalon ($d = 0.88$ mm). The light exiting the étalon is focused onto the CMOS sensor via the field lens ($f_2 = 150$ mm) as concentric rings due to the interference condition [Eq. (1)]. All lenses are 50.8 mm in diameter and the camera is a 24 MP Nikon D5200 DSLR.

A. Image processing

1. Define the model

The model for intensity on the sensor is a function of wavelength and pixel distance relative to the center of the concentric rings. To increase signal-to-noise and decrease the number of pixels (24×10^6) in the calculation, a technique called annular summing^{19,20} is used where pixels are binned into annuli with equal area. Each pixel in a bin can be treated as an independent identically distributed measurement because the count rate on a particular pixel is uncorrelated with other pixels. For each annuli, the mean and standard deviation are calculated from the histogram of points in an annulus to account for differences in the number of pixels in each annulus from mapping discrete pixels to annuli. Pixels that have counts outside ± 3 standard deviations from the mean are treated as outliers and discarded. Before the final annular sum can be analyzed, the center of the ring pattern must be known to within a few tenths of a pixel. The center is determined by iteratively performing annular sums on halves of the CCD based on an initial center-of-mass estimate. A new center guess is calculated based on the misalignment of the individual peaks. This procedure is iterated until a threshold for the next step size is met. A portion of an annular sum is shown compared against the raw pixel intensities in Fig. 4. The expected noise is mostly from photon counting statistics. The read noise and

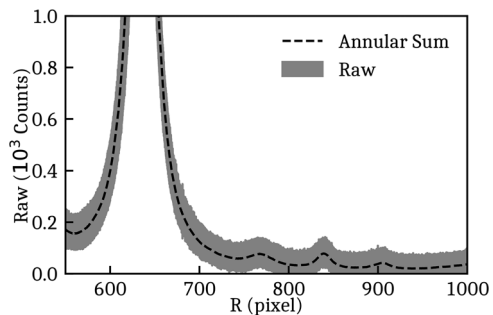


FIG. 4. Intensity in counts is shown as a function of radius from the center of the ring pattern. The noise is the result of mostly photon counting statistics. The read noise and dark counts are on the order of a few counts. Annular summing reduces the uncertainty of the mean counts in a bin to approximately 1 count.

dark counts are on the order a few counts each. With annular summing, small features and overlapping peaks are identifiable with a significant increase in signal to noise ($\approx 50\times$).

B. Wavelength and point spread function calibration

Calibration of a Fabry-Pérot spectrometer with fixed spacing and stable cavity pressure requires knowing the étalon spacing, d , and the camera focal length, f_2 , for an absolute wavelength calibration and the finesse, \mathcal{F} , for the instrument point spread function. The absolute wavelength calibration is performed using spectroscopic methods because it is impossible to measure the étalon spacing to within $\lambda/2$ to determine the absolute order number, m_0 . Normally, the étalon spacing is calibrated by placing the étalon in a chamber and scanning the pressure to vary the index of refraction. The exact spacing is not known during the pressure scan, but the change in spacing is known very precisely.²¹ Our constraints on time resolution where the entire spectra is measured simultaneously makes the pressure scanning technique impossible to implement and requires a fixed étalon spacing calibration procedure. The maximum possible finesse can be calculated from the reflectivity of the interior surfaces of the étalon, but the effective finesse depends on other factors such as plate flatness, the parallelism of the plates, and the clear aperture.

The calibration procedure involves solving for f_2 , d , and the finesse \mathcal{F} by forward modeling the spectra from a thorium hollow cathode lamp with argon gas fill measured by the Fabry-Pérot spectrometer. Thorium was chosen because it is a heavy element with only one long-lived isotope allowing for simultaneous wavelength and point-spread function calibrations. The point-spread function, PSF, is given by

$$\text{PSF}(\lambda) = \left(1 + \left[\frac{2\mathcal{F}}{\pi} \sin \left(\pi \frac{2nd \cos \theta}{\lambda} \right) \right]^2 \right)^{-1}. \quad (2)$$

The point-spread function can easily be mapped to pixel radius r by using the following trigonometric relationship:

$$\cos \theta = \frac{f_2}{\sqrt{f_2^2 + r^2}}. \quad (3)$$

Finding the étalon spacing d to the precision needed is difficult because the uncertainties in the measurements lead to finding many solutions corresponding to adjacent order numbers. To solve this issue, a Bayesian approach called multimodal nested sampling is used, which is encoded in the software package MultiNest^{22–25} which was adapted from the nested sampling algorithm.²⁶ This method finds the probability distribution which best describes the uncertainty in the calibration parameters conditioned upon background information that constrains the reasonable range for these parameters. Our analysis uses highly informed prior information to limit the scope of the Monte Carlo search since it is a computationally expensive procedure.

The goal of calibration is to calculate the marginal posterior probability distribution for f_2 , d , and \mathcal{F} , given a hollow-cathode lamp spectrum. The model for the calibration spectrum consists of 6 parameters: the camera focal length, f_2 , the étalon spacing, d , the finesse, \mathcal{F} , the Ar II amplitude A , the Th I amplitude relative to the Ar II amplitude A_{rel} , and the Ar II temperature, T_i . The thorium

temperature is assumed to be 1000 K,²⁷ however, the modeled spectrum shows very little change when varying the temperature from room temperature up to 2000 K. These calibration parameters will be noted as θ_C for brevity. As noted in Fig. 5, three filters are used to limit the contribution from nearby Th I peaks so that the tails of the dominant lines due to the Lorentzian point-spread function can be distinguished. The goal of performing the calibration is to acquire sufficiently precise data to minimize the uncertainty in f_2 , d , and \mathcal{F} . The marginal posterior probability distribution for these calibration parameters is given by

$$p(f_2, d, \mathcal{F} | \{C_r\}, I) = \int p(\theta_C | \{C_r\}, I) dA dA_{\text{rel}} dT_i, \quad (4)$$

where $\{C_r\}$ represents the set of calibration measurements at each radii, I is any additional background information such as known wavelengths, and $p(\theta_C | \{C_r\}, I)$ is the posterior probability distribution including extra parameters, such as amplitudes, needed for modeling the spectrometer image of the calibration lamp spectra. The full marginal posterior in Eq. (4) can be rewritten using Bayes' theorem^{28,29} as

$$p(\theta_C | \{C_r\}, I) = \frac{p(\{C_r\} | \theta_C, I) p(\theta_C | I)}{p(\{C_r\} | I)}, \quad (5)$$

where $p(\{C_r\} | \theta_C, I)$ is the likelihood, $p(\theta_C | I)$ is the prior probability, and $p(\{C_r\} | I)$ is the evidence. We follow the flowchart in Fig. 3 to determine the calibration parameters and their uncertainties from $p(\theta_C | \{C_r\}, I)$.

1. Define the prior

The prior probability consists of 6 independent uniform distributions—one for each parameter. The prior distribution used for f_2 is a uniform distribution between [145.5, 154.5] mm which assumes with high confidence that f_2 is within three standard deviations of the manufacturer's specification of 150 ± 1.5 mm. The prior probability range for d is determined by back-lighting the étalon with a Hg lamp and counting the number of fringe orders that pass as the alignment screws are adjusted. Estimating 40 orders at 500 nm

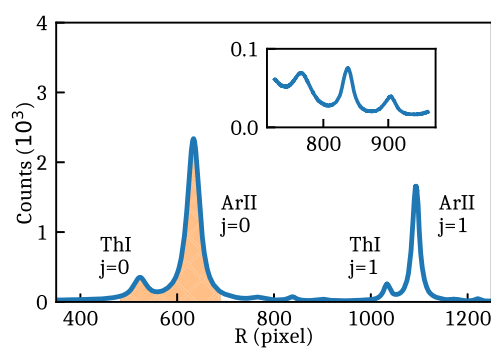


FIG. 5. Annular sum of the Th-Ar hollow cathode lamp using the 3 Andover 1 nm FWHM bandpass filters at 488 nm to reduce contributions from weak Th I lines. A Th I line (487.873 302 nm) and an Ar II line (487.986 34 nm) have been identified for their first and second relative order numbers. The orange region represents a calibration fit and shaded for emphasis. Inset: The central peak is a Th I line (487.800 942 nm). The two remaining peaks are thought to consist of multiple unresolved lines.

yields a shift in d of 0.01 mm giving a range of [0.87, 0.89] mm. The lower bound for the finesse is set by calculating the ratio of the distance between adjacent Ar II orders in pixels-squared and the full-width half-maximum in pixels squared. The upper bound for the finesse prior is set by estimating the ideal finesse from the reflectivity of the coating (92%).³⁰ Combining these results gives us the expectation that the finesse lies in the range [20, 32]. The prior ranges for the amplitudes are set using a lower bound of 75% and an upper bound of 200% of the counts at the peak location. Very little is known about the specific conditions of the plasma inside the hollow cathode calibration lamp. A relatively naive uniform prior for the argon ion temperature ranging from room temperature to 1 eV was used. This prior for T_i is justified *post facto* since the resulting marginal posterior is Gaussian in shape and well within the prior boundaries.

2. Define the likelihood

The last component needed for calculating the marginal posterior is the likelihood probability distribution. Since each data point in $\{C_r\}$ is characterized by a Gaussian uncertainty, a maximum entropy argument²⁹ for assigning a particular distribution yields a χ^2 -distribution. Each pixel is an independent measurement resulting in

$$p(\theta_C|\{C_r\}, I) = \prod_{r=1}^N \frac{1}{\sigma_r \sqrt{2\pi}} \exp \left[-\frac{(C_r - M_C(r))^2}{2\sigma_r^2} \right], \quad (6)$$

where $M_C(r)$ is the calibration forward model for the lamp spectrum and σ_r is the uncertainty associated with the data point C_r .

3. Calculate posterior and marginalize parameters

To verify the calibration procedure, a synthetic calibration image with just two dominant peaks was generated using $f_2 = 150$ mm, $d = 0.88$ mm, and $\mathcal{F} = 20.7$ for the focal length, étalon spacing, and finesse, respectively. Noise was then added to the image based on photon counting statistics. The synthetic image was processed by the procedure outlined in Sec. III A. The marginal posterior results are shown in Figs. 6 and 7. The joint marginal distribution for f_2 and d highlights the need for multimodal nested sampling. The bin widths for the d axis are $\lambda/10$ to show there are many possible solutions within our precision. The peaks are separated by $\lambda/2$ which corresponds to a different maximum order, m_0 . There is also a positive correlation with f_2 as d is increased to the next order solution. It should be noted that this is a difficult problem to solve because of the many solutions and many regions of low likelihood. This solution was run on 240 processors with 1000 live points sampling over a 150×10^6 points from the prior probability space with only 47 452 accepted points and took approximately 18 h to complete. Once a calibration is performed, determining the plasma flow velocity and ion temperature is much less computationally intensive.

C. Plasma analysis

The analysis of a plasma is performed in a manner similar to the calibration. Ultimately, the goal is to calculate the marginal posterior for T_i and V , given emission measurements from the plasma. This is accomplished by marginalizing over the nuisance parameters (such

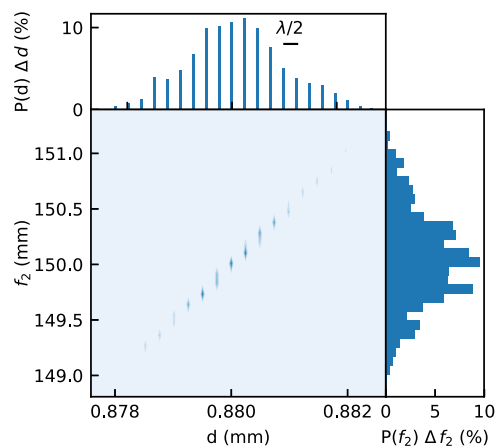


FIG. 6. Marginal posterior probabilities for focal length f_2 and étalon spacing d for a synthetic calibration. The empty space in the d posterior displays the discrete separation by $\lambda/2$ for the possible solutions to the maximum order number. The synthetic image was created using 150 mm and 0.88 for f_2 and d , respectively.

as the amplitude, A) and the calibration resulting in

$$P(T_i, V|\{P_r\}, I) = \int_V P(\theta_P, \theta_C|\{P_r\}, \{C_r\}, I) d\theta_C dA, \quad (7)$$

where θ_P are the plasma model parameters, $\{P_r\}$ are the intensity measurements from a plasma image, and $P(\theta_P, \theta_C|\{P_r\}, \{C_r\}, I)$ is the joint probability of the plasma model parameters and the calibration parameters conditioned upon all of the measurements. The integrand in Eq. (7) can be rewritten as

$$P(\theta_P, \theta_C|\{P_r\}, \{C_r\}, I) = P(\theta_P|\{P_r\}, \theta_C, I) P(\theta_C|\{C_r\}, I), \quad (8)$$

where $P(\theta_P|\{P_r\}, \theta_C, I)$ is the marginal posterior for the plasma parameters given the calibration parameters and $P(\theta_C|\{C_r\}, I)$ is the calibration marginal posterior determined in Sec. III B. The marginal posterior for the plasma parameters will be computed using MultiNest.

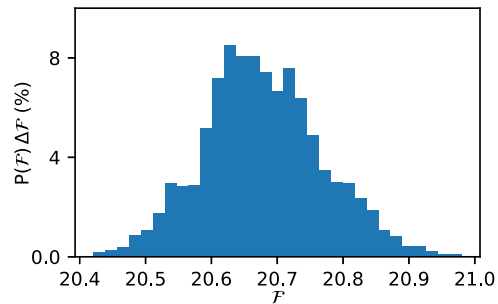


FIG. 7. Marginal posterior probability for the finesse, \mathcal{F} , from a synthetic calibration generated with a true value of 20.7. Marginal posterior is mostly Gaussian in shape and can be described by a mean and standard deviation of 20.68 and 0.09, respectively.

The posterior for the plasma parameters given a calibration can be rewritten using Bayes' theorem as

$$P(\theta_P | \{P_r\}, \theta_C, I) = \frac{P(\{P_r\} | \theta_P, \theta_C, I) P(\theta_P | I)}{P(\{P_r\} | \theta_C, I)}, \quad (9)$$

where $P(\{P_r\} | \theta_P, \theta_C, I)$ is the likelihood probability distribution, $P(\theta_P | I)$ is the prior distribution for the plasma parameters, and $P(\{P_r\} | \theta_C, I)$ is the evidence. The likelihood is the same as Eq. (6) with a plasma forward model for the annular bin counts $M_P(r)$ given by

$$M_P(r) = \int d\lambda \text{PSF}(\lambda) \times A \exp \left[-\frac{1}{2} \left(\frac{\lambda - \lambda_0(1 - V/c)}{\sigma_{T_i}} \right)^2 \right], \quad (10)$$

where λ_0 is the wavelength of the Ar II line, V is the toroidal velocity, A is the amplitude, and σ_{T_i} is the thermal broadening. For now, chord effects are neglected for simplicity of analysis. Future work will incorporate a velocity gradient along the line-of-sight in the forward model and multiple chord measurements will be used to resolve the velocity gradient. The prior range for T_i is between room temperature and the electron temperature since the only ion heating mechanism is through electron collisions. The prior range for V is likewise assumed to be subsonic ($|V| < \sqrt{kT_e/m_i}$). The prior range for the amplitude is set at 75% and 200% of the peak counts in the image.

IV. PRELIMINARY RESULTS

A calibration for measuring Ar II emission was taken using 3 stacked 1 nm full-width half-maximum 488 nm central wavelength filters with an integration time of 3 s. The resulting image is shown in Fig. 1 with a log-scale for the counts. Most of the extraneous lines have been reduced to just above the background level as shown in Fig. 5. Performing the calibration procedure outlined in Sec. III B yielded poor results for the wavelength calibration. As a

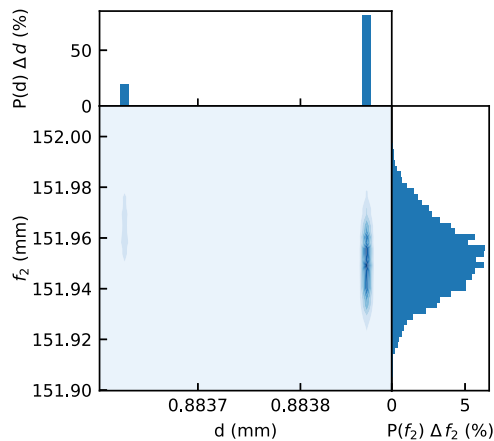


FIG. 8. Marginal joint posterior probabilities for f_2 and d from a calibration lamp image using a model with 3 wavelengths each with one order. The probability distributions are better constrained than the synthetic results due to the third wavelength used in the model. The estimated systematic uncertainty in the wavelength calibration can be characterized by a Doppler shift of 20 m/s for the ArII line.

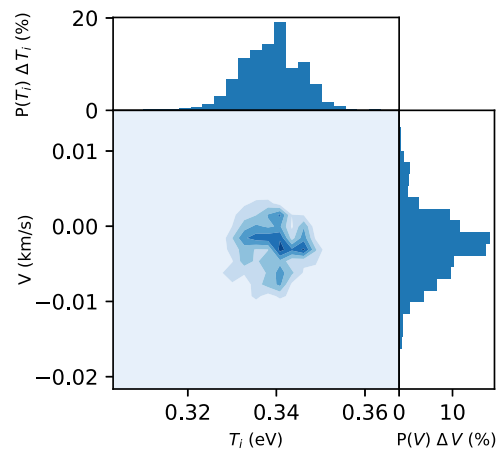


FIG. 9. Marginal joint posterior probabilities for T_i and V from an argon plasma on the PCX experiment. The plasma was generated using a single LaB6 cathode. The spectrometer chord was near the axis of symmetry where the toroidal flow velocity must go to zero. The marginal probabilities resemble Gaussian distributions, and the marginal joint posterior shows very little correlation.

solution, a known third emission line was added to the calibration. The middle nuisance peak in the inset of Fig. 5 is identified as a singlet from the NIST Atomic Spectra Database¹⁸ using the posterior wavelength calibration with two known lines. The resulting posterior distributions using 3 emission lines for f_2 and d are shown in Fig. 8. All other marginal posterior distributions resemble Gaussian distributions and can be characterized by a mean and standard deviation. The finesse was measured to be 22.71 ± 0.04 . The addition of the third wavelength in the calibration significantly constrains the marginal posterior for the étalon spacing. Any errors in the absolute wavelength calibration result in a systematic offset for the velocity. Refitting the Ar II peak with a velocity shift yields a systematic error of 20 m/s.

Initial data for the Fabry-Pérot spectrometer were taken on the plasma Couette experiment (PCX).^{5,31,32} Plasmas were created with a lanthanum hexaboride (LaB6) emissive cathode^{16,33} placed in the center and biased relative to a grounded molybdenum anode to produce an argon plasma with an electron density of $4 \times 10^{17} \text{ m}^{-3}$ and an electron temperature of 4 eV. Using the marginalized calibration posterior for f_2 , d , and \mathcal{F} in the analysis outlined in Sec. III C, preliminary results show an ion temperature of 0.339 ± 0.007 eV and an ion velocity of -3 ± 4 m/s for a chord very close to the axis of symmetry for the vessel where no flow is expected because of the regularity condition at $r = 0$. The marginal joint posterior probabilities for T_i and V can be seen in Fig. 9. Initial results from a volumetric flow drive (VFD)³⁴ plasma on PCX measured ion velocities of 250 m/s.

V. CONCLUSION

A Fabry-Pérot spectrometer has been built to measure ion temperatures and velocities for studying plasma hydrodynamics. A calibration procedure for absolute wavelength and point-spread function was developed using Bayesian methods. With the calibration, ion temperatures are measured with an uncertainty less than 0.01 eV and statistical velocity uncertainties less than 10 m/s with a

systematic uncertainty less than 20 m/s. Stationary plasmas on PCX have been measured with the spectrometer. The diagnostic is now ready to measure multiple chords to diagnose the full velocity profile.

ACKNOWLEDGMENTS

The authors would like to thank C. M. Cooper and F. L. Roesler for their contribution to the initial construction and operation of the Fabry-Pérot spectrometer. This material is based on the work supported by the U.S. Department of Energy, Office of Science, Office of Fusion Energy Science under Award No. DE-SC0008709 and supported by the National Science Foundation under Grant Nos. PHY 0923258, AST-1518115, and AST-1211937. Grant No. PHY 0923258 was funded under the American Recovery and Reinvestment Act of 2009 (ARRA).

REFERENCES

- ¹S. D. Baalrud, B. Scheiner, B. Yee, M. Hopkins, and E. Barnat, "Extensions and applications of the Bohm criterion," *Plasma Phys. Controlled Fusion* **57**, 044003 (2015).
- ²S. Robertson, "Sheath and presheath in plasma with warm ions," *Phys. Plasmas* **16**, 103503 (2009).
- ³M. Keidar, A. Shashurin, O. Volotskova, M. Ann Stepp, P. Srinivasan, A. Sandler, and B. Trink, "Cold atmospheric plasma in cancer therapy," *Phys. Plasmas* **20**, 057101 (2013).
- ⁴S. Braginskii, "Transport processes in a plasma," in *Reviews of Plasma Physics*, edited by M. A. Leontovich (Consultants Bureau, New York, 1965), Vol. 1, p. 250.
- ⁵C. Collins, N. Katz, J. Wallace, J. Jara-Almonte, I. Reese, E. Zweibel, and C. B. Forest, "Stirring unmagnetized plasma," *Phys. Rev. Lett.* **108**, 115001 (2012).
- ⁶P. C. Stangeby, "Measuring plasma drift velocities in tokamak edge plasmas using probes," *Phys. Fluids* **27**, 2699 (1984).
- ⁷B. J. Peterson, J. N. Talmadge, D. T. Anderson, F. S. B. Anderson, and J. L. Shohet, "Measurement of ion flows using an 'unmagnetized' Mach probe in the interchangeable module stellarator," *Rev. Sci. Instrum.* **65**, 2599–2606 (1994).
- ⁸E. Ko and N. Hershkowitz, "Asymmetry reversal of ion collection by Mach probes in flowing unmagnetized plasmas," *Plasma Phys. Controlled Fusion* **48**, 621–634 (2006).
- ⁹I. H. Hutchinson, "Ion collection by a sphere in a flowing plasma: 2. Non-zero Debye length," *Plasma Phys. Controlled Fusion* **45**, 1477–1500 (2003).
- ¹⁰D. L. Rudakov, M. G. Shats, R. W. Boswell, C. Charles, and J. Howard, "Overview of probe diagnostics on the H-1 heliac," *Rev. Sci. Instrum.* **70**, 476–479 (1999).
- ¹¹C. Charles, A. W. Degeling, T. E. Sheridan, J. H. Harris, M. A. Lieberman, and R. W. Boswell, "Absolute measurements and modeling of radio frequency electric fields using a retarding field energy analyzer," *Phys. Plasmas* **7**, 5232–5241 (2000).
- ¹²Z. Harvey, S. Chakraborty Thakur, A. Hansen, R. Hardin, W. S. Przybysz, and E. E. Scime, "Comparison of gridded energy analyzer and laser induced fluorescence measurements of a two-component ion distribution," *Rev. Sci. Instrum.* **79**, 10F314 (2008).
- ¹³R. A. Stern and J. A. Johnson, "Plasma ion diagnostics using resonant fluorescence," *Phys. Rev. Lett.* **34**, 1548–1551 (1975).
- ¹⁴M. J. Goeckner, J. Goree, and T. E. Sheridan, "Laserinduced fluorescence characterization of a multidipole filament plasma," *Phys. Fluids B* **3**, 2913–2921 (1991).
- ¹⁵G. D. Severn, D. A. Edrich, and R. McWilliams, "Argon ion laser-induced fluorescence with diode lasers," *Rev. Sci. Instrum.* **69**, 10–15 (1998).
- ¹⁶C. B. Forest, K. Flanagan, M. Brookhart, M. Clark, C. M. Cooper, V. Desangles, J. Egedal, D. Endrizzi, I. V. Khalzov, H. Li, M. Miesch, J. Milhone, M. Nornberg, J. Olson, E. Peterson, F. Roesler, A. Schekochihin, O. Schmitz, R. Siller, A. Spitkovsky, A. Stemo, J. Wallace, D. Weisberg, and E. Zweibel, "The Wisconsin plasma astrophysics laboratory," *J. Plasma Phys.* **81**, 345810501 (2015).
- ¹⁷C. M. Cooper, D. B. Weisberg, I. Khalzov, J. Milhone, K. Flanagan, E. Peterson, C. Wahl, and C. B. Forest, "Direct measurement of the plasma loss width in an optimized, high ionization fraction, magnetic multi-dipole ring cusp," *Phys. Plasmas* **23**, 102505 (2016).
- ¹⁸A. Kramida, Y. Ralchenko, J. Reader, and N. A. Team, NIST Atomic Spectra Database (version 5.6.1), 2018.
- ¹⁹M. M. Coakley and F. L. Roesler, "Application of conventional CCD cameras with Fabry-Perot spectrometers for airglow observations," *Proc. SPIE* **2266**, 122 (1994).
- ²⁰M. M. Coakley, F. L. Roesler, R. J. Reynolds, and S. Nossal, "Fabry-Perot CCD annular-summing spectroscopy: Study and implementation for aeronomy applications," *Appl. Opt.* **35**, 6479 (1996).
- ²¹F. Roesler, "Fabry-Perot instruments for astronomy," in *Methods in Experimental Physics* (Academic Press, 1974), Vol. 12, pp. 531–569.
- ²²F. Feroz, M. P. Hobson, and M. Bridges, "MultiNest: An efficient and robust Bayesian inference tool for cosmology and particle physics," *Mon. Not. R. Astron. Soc.* **398**, 1601–1614 (2009).
- ²³F. Feroz and M. P. Hobson, "Multimodal nested sampling: An efficient and robust alternative to Markov chain Monte Carlo methods for astronomical data analyses," *Mon. Not. R. Astron. Soc.* **384**, 449–463 (2008).
- ²⁴F. Feroz, M. P. Hobson, E. Cameron, and A. N. Pettitt, "Importance nested sampling and the MultiNest algorithm," (2013); e-print [arXiv:1306.2144](https://arxiv.org/abs/1306.2144).
- ²⁵J. Buchner, A. Georgakakis, K. Nandra, L. Hsu, C. Rangel, M. Brightman, A. Merlini, M. Salvato, J. Donley, and D. Kocevski, "X-ray spectral modelling of the AGN obscuring region in the CDFs: Bayesian model selection and catalogue," *Astron. Astrophys.* **564**, A125 (2014).
- ²⁶J. Skilling, "Nested sampling for general Bayesian computation," *Bayesian Anal.* **1**, 833–859 (2006).
- ²⁷Based on correspondence with F. L. Roesler.
- ²⁸U. von Toussaint, "Bayesian inference in physics," *Rev. Mod. Phys.* **83**, 943–999 (2011).
- ²⁹D. Sivia and J. Skilling, *Data Analysis: A Bayesian Tutorial* (Oxford University Press, Oxford, United Kingdom, 2006).
- ³⁰J. T. Trauger, "Broadband dielectric mirror coatings for Fabry-Perot spectroscopy," *Appl. Opt.* **15**, 2998 (1976).
- ³¹C. Collins, M. Clark, C. M. Cooper, K. Flanagan, I. V. Khalzov, M. D. Nornberg, B. Seidlitz, J. Wallace, and C. B. Forest, "Taylor-Couette flow of unmagnetized plasma," *Phys. Plasmas* **21**, 042117 (2014).
- ³²N. Katz, C. Collins, J. Wallace, M. Clark, D. Weisberg, J. Jara-Almonte, I. Reese, C. Wahl, and C. Forest, "Magnetic bucket for rotating unmagnetized plasma," *Rev. Sci. Instrum.* **83**, 063502 (2012).
- ³³C. M. Cooper, J. Wallace, M. Brookhart, M. Clark, C. Collins, W. X. Ding, K. Flanagan, I. Khalzov, Y. Li, J. Milhone, M. Nornberg, P. Nonn, D. Weisberg, D. G. Whyte, E. Zweibel, and C. B. Forest, "The Madison plasma dynamo experiment: A facility for studying laboratory plasma astrophysics," *Phys. Plasmas* **21**, 013505 (2014).
- ³⁴D. B. Weisberg, E. Peterson, J. Milhone, D. Endrizzi, C. Cooper, V. Désangles, I. Khalzov, R. Siller, and C. B. Forest, "Driving large magnetic Reynolds number flow in highly ionized, unmagnetized plasmas," *Phys. Plasmas* **24**, 056502 (2017).